Ewald construction and resolution function for rocking-curve small-angle neutron scattering experiments

Nikolaos Daniilidis,* Ivo Dimitrov and Xinsheng Sean Ling

Department of Physics, Brown University, Box 1843, Providence, RI 02912, USA. Correspondence e-mail: nikos@brown.edu

A geometrical Ewald construction for small-angle neutron scattering experiments from line-like objects with a preferential orientation of the lines, such as flux-line lattices in type-II superconductors, is described. The Ewald construction offers a straightforward way to interpret rocking-curve experiments. It allows calculation of the resolution function in rocking-curve measurements. The resolution function for a given instrumental geometry can be readily computed by performing two numerical integrations.

1. Introduction

Small-angle neutron scattering (SANS) is a valuable tool in studying the structures of the Abrikosov flux line lattices (FLLs) (Christen et al., 1980). In order to extract detailed information for the structure function from the scattering data, the instrumental resolution function has to be considered. Several authors (Roth & Lewit-Bentley, 1982; Schoenborn, 1983; Ramakrishnan, 1985; Pedersen et al., 1990; Barker & Pedersen, 1995) have considered resolution functions which are applicable under various different experimental conditions, with the emphasis placed on Gaussian approximations. The complete three-dimensional resolution function for small-angle scattering measurements has been calculated analytically using the Gaussian approximation (Cubitt et al., 1992; Harris et al., 1995) and numerically using Monte Carlo simulations (Harris et al., 1995).

In rocking-curve measurements of FLLs, in which an FLL is rotated with respect to the neutron beam, the flux-line translational correlations in the direction of the magnetic field (i.e. longitudinal) are probed. These measurements provide considerably higher resolution than that in the transverse (perpendicular to the magnetic field) direction. In these cases, an accurate assessment of the instrumental resolution is crucial for the deconvolution of the structure function from the measured intensity profiles. A method to determine the actual resolution function beyond the level of accuracy provided by the Gaussian approximation (Harris et al., 1995) is needed. For example, it has been noted in the Monte Carlo simulation of Harris et al. (1995) that the typical resolution function for rocking-curve measurements resembles a box-shaped function, which is poorly approximated in the Gaussian treatment. This discrepancy is most significant when studying systems where the intrinsic width of the diffraction peaks is close to the instrumental resolution limit. As an example, the FLLs in ultrapure superconducting samples (Lynn et al., 1994; Yaron et al., 1994; Ling et al., 2001; Klein et al., 2001; Forgan et al., 2002) can give diffraction peaks that are resolution limited, or close to the resolution limit. Ideally, one would want to determine the resolution function for a given instrumental configuration by using direct measurements of the neutron-beam collimation profile and the wavelength spread. Here we describe a method for obtaining the resolution function for rocking-curve measurements, starting from the neutron-beam collimation profile and wavelength spread. The calculation is simple, involving just two numerical integrations. As an example of this procedure, we compute the resolution function for a given instrumental configuration of the 30 m NG-3 instrument at NCNR-NIST, which employs a mechanical velocity selector and double pinhole collimation (Glinka et al., 1998). We compare these results with measured rocking curves, close to the resolution limit, obtained on an FLL in niobium. The procedure we describe is built upon the Ewald construction, as applied to SANS on FLLs (Christen et al., 1980; Yaron et al., 1994). The same description applies to diffraction from any medium consisting of line-like objects with a preferred average orientation of the lines and is useful in understanding various aspects of small-angle diffraction by such systems. In specific, the Ewald construction offers a straightforward way to determine how different experimental parameters such as sample orientation, beam collimation, and wavelength spread affect the diffraction condition.

2. Scattering geometry

We consider a typical small-angle scattering geometry, shown in Fig. 1, in which the neutron beam traverses the sample. The two-dimensional position-sensitive detector is located at a certain distance from the sample, on the side where both the direct neutron beam and diffracted neutrons emerge. The diffracting line-objects have a preferred direction which is controlled by an external parameter, such as the applied magnetic field in the case of FLLs. The orientation of the line-objects is rotated with respect to the incoming neutron beam by an angle ω. In the case of an FLL, both the sample and magnetic field (in reality the entire magnet cryostat) are rotated with
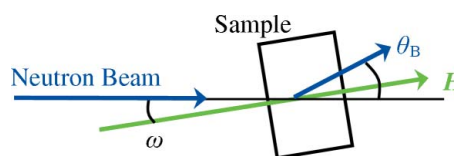

Figure 1
Scattering geometry in SANS measurements. The sample and magnetic field (thus, the flux-line lattice) are rotated by ω with respect to the incident neutron beam. The diffracted neutrons satisfy the Bragg condition at angles θ_B.

short communications

respect to the beam. This rotation is necessary for the sensitive alignment required to optimize the scattering conditions, but also useful in performing rocking-curve measurements. In these, the diffracting lattice of line-objects is rotated with respect to the beam by ω, in a stepwise fashion. The intensity of a given Bragg peak varies with ω. This variation contains information about the longitudinal, parallel to the field, structure function of the lattice.

In what follows we will use two coordinate systems. The instrument-fixed frame is chosen such that the neutron beam travels in the $-\mathbf{z}$ direction and the position-sensitive detector lies on the xy plane, with $\mathbf{x}$ denoting the horizontal direction. In addition, we use a sample-fixed coordinate system, denoted by tilded symbols $\tilde{x}_i$. The orientation of the tilded coordinates is such that the average orientation of the line-objects (e.g. the magnetic field) is in the $\tilde{\mathbf{z}}$ direction, while the $\tilde{\mathbf{x}}$ and $\tilde{\mathbf{y}}$ axes are chosen to be respectively parallel to the $\mathbf{x}$ and $\mathbf{y}$ axes when $\mathbf{z} \| \tilde{\mathbf{z}}$. In other words, the tilded coordinates are rotated by ω with respect to the non-tilded ones (Fig. 1). In practical situations, the rotation is about the vertical $\mathbf{y}$ axis and this will be the case we consider.
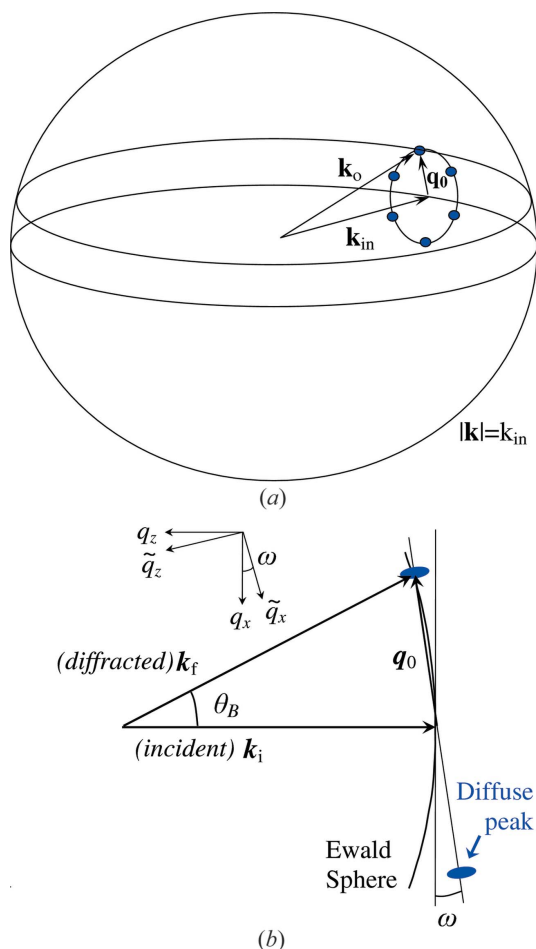

(a)

(b)

Figure 2
(a) Ewald construction for neutron scattering from an FLL. The Ewald sphere has radius $|\mathbf{k}| = k_{in}$ and is centered at $(0, 0, -k_{in})$. The first-order reciprocal-lattice points of a hexagonal lattice are shown. A Bragg peak at scattering vector $\mathbf{q}_0$ appears when the corresponding reciprocal-lattice point intersects the Ewald sphere. (b) Construction corresponding to the geometry of Fig. 1, simplified to a two-dimensional sketch. The diffuse reciprocal-lattice peaks of an FLL are in reality compressed along the q_z direction due to the flux-lattice elastic moduli. Here we present them elongated for ease of presentation.

3. Ewald construction for a perfectly parallel and monochromatic beam

The Ewald construction in (reciprocal) $\mathbf{q}$ space offers a straightforward way to interpret scattering patterns from line-object lattices. The reciprocal lattice of an ordered array of infinitely long straight lines is a set of points on a two-dimensional plane. By our choice of tilded coordinates, this is the $\tilde{q}_x \tilde{q}_y$ plane. For a disordered line lattice, long-range order is lost in all three directions; the reciprocal-lattice points become diffuse three-dimensional objects, each one centered at the position of a reciprocal-lattice point of the ideal lattice. Values of momentum transfer corresponding to these points will satisfy the Bragg condition. When interference occurs, the intensity at a given point in $\mathbf{q}$ space is determined by the structure function, $S(\mathbf{q})$, of the lattice. Interference occurs whenever the Bragg condition can be satisfied for a given scattering geometry. This is expressed geometrically by constructing a sphere in $\mathbf{q}$ space, centered on $(0, 0, -k_{in})$, with radius $|\mathbf{q}| = k_{in} = 2\pi/\lambda$, with λ the neutron wavelength. This is shown in Fig. 2(a). This is the Ewald sphere and describes the locus of diffracted neutron momenta consistent with momentum conservation.[1] Diffraction occurs whenever a reciprocal-lattice peak intersects the Ewald sphere.

For the geometry represented in Fig. 1, the Ewald sphere is centered on $(q_x, q_y, q_z) = (0, 0, -k_{in})$ and the reciprocal lattice is rotated by ω around the $\mathbf{q}_y$ axis. The tilded axes $(\tilde{q}_x, \tilde{q}_y, \tilde{q}_z)$, rotated by ω around $\mathbf{q}_y$ (Fig. 2), serve to identify peaks of the rotated reciprocal lattice. This situation is depicted schematically in Fig. 2(b). We consider a point in reciprocal space, with coordinates in the tilded axes given by

$$(\tilde{q}_{x0}, \tilde{q}_{y0}, \tilde{q}_{z0}) = (Q_0 \cos \tilde{\varphi} \sin \tilde{\theta}, \ Q_0 \sin \tilde{\varphi} \sin \tilde{\theta}, \ Q_0 \cos \tilde{\theta}). \quad (1)$$

Here the angles $\tilde{\theta}$ and $\tilde{\varphi}$ are the usual polar and azimuthal angles in the tilded coordinate system. The location of this point in the unrotated axes is

$$q_{x0} = \tilde{q}_{x0} \cos \omega + \tilde{q}_{z0} \sin \omega \simeq \tilde{q}_{x0} + \tilde{q}_{z0} \omega, \quad (2)$$

$$q_{y0} = \tilde{q}_{y0}, \quad (3)$$

$$q_{z0} = -\tilde{q}_{x0} \sin \omega + \tilde{q}_{z0} \cos \omega \simeq -\tilde{q}_{x0} \omega + \tilde{q}_{z0}, \quad (4)$$

to first order in ω. In the case of FLLs, the structure function is sharp in the longitudinal (q_z) direction. The typical width $\Delta \tilde{q}_z$ is considerably smaller than the reciprocal-lattice peak spacing $\tilde{q}_{x0,y0} = O(Q_0)$. Consequently the regions of interest in reciprocal space satisfy $\tilde{q}_{z0} \ll \tilde{q}_{x0,y0}$, so that the variation of q_{x0} by $\delta q_{x0} = O(\tilde{q}_{z0} \omega)$ in equation (2) above can be neglected.

These expressions elucidate how the rotation of the sample allows us to obtain the longitudinal behavior, along q_z, of the line-lattice structure function. Consider a specific Bragg peak and integrate out the intensity on the $q_x q_y$ plane. Then, a variation in ω leads to variation in the reciprocal lattice $\tilde{q}_z$ intersecting the Ewald sphere. The intensity profile obtained is, to first order, approximated by $I(\omega) \propto \overline{S}(\tilde{q}_z = \tilde{q}_{x0} \omega)$, where the overbar denotes integration in the transverse ($\tilde{q}_x \tilde{q}_y$) plane.

4. Treatment of the resolution function

The instrumental resolution function is determined by the incident-beam wavelength spread and collimation. In the previous section we described the Ewald construction for a perfectly parallel and

---

[1] We can safely disregard the minute fuzziness of the Ewald sphere introduced by inelastic scattering processes.

monochromatic beam. For a realistic beam this has to be modified. Variations in the incident beam direction lead to rotations of the Ewald sphere with respect to the reciprocal lattice. Wavelength spread leads to a variation of the size of the Ewald sphere. The scattering pattern is the combined result of several different Ewald constructions with varying Ewald sphere sizes and orientations of reciprocal lattice with respect to the sphere. The instrumental resolution function in the rocking-curve measurement corresponds to the intensity $R(\omega)$ that would be obtained as a function of rotation angle, ω, from a $\delta(\mathbf{q} - \mathbf{q}_0)$ peak in the reciprocal lattice. In what follows we will calculate resolution functions up to a normalization constant which can be determined by the normalization condition $\int R(\omega) \, \mathrm{d}\omega = 1$.

4.1. Beam collimation

The incident-beam collimation is described by an angular intensity profile $I_0(\theta, \varphi)$, which can be directly measured. Here θ and φ are polar and azimuthal angles in instrument-fixed spherical coordinates. Ideally, for double pinhole collimation and neglecting the effect of gravity on a non-monochromatic beam, the profile does not depend on azimuthal angle: $I_0 = I_0(\theta)$. The parts of the incident beam with different directions correspond to different Ewald constructions. Each one will give rise to diffracted intensity from the δ peak at a slightly different rotation angle ω, thus giving rise to an intensity profile $I(\omega)$.

We include the effect of beam imperfect collimation by allowing the reciprocal lattice to rotate with respect to the Ewald sphere. The rotation is by θ_1 about $\tilde{\mathbf{q}}_y$ and then by θ_2 about the rotated $\tilde{\mathbf{q}}_x'$. The combined effect on the point at $(\tilde{q}_{x0}, \tilde{q}_{y0}, \tilde{q}_{z0})$ results in $(\tilde{q}_{x0}'', \tilde{q}_{y0}'', \tilde{q}_{z0}'')$, given by

$$\tilde{q}_{x0}'' = \tilde{q}_{x0} \cos \theta_1 - \tilde{q}_{z0} \sin \theta_1,$$

$$\tilde{q}_{y0}'' = \tilde{q}_{x0} \sin \theta_1 \sin \theta_2 + \tilde{q}_{y0} \cos \theta_2 + \tilde{q}_{z0} \cos \theta_1 \sin \theta_2,$$

$$\tilde{q}_{z0}'' = \tilde{q}_{x0} \sin \theta_1 \cos \theta_2 - \tilde{q}_{y0} \sin \theta_2 + \tilde{q}_{z0} \cos \theta_1 \cos \theta_2.$$

In practice, the angles θ_1, θ_2 are small and we can expand the above to first order in these angles. In addition, we take into account the condition $\tilde{q}_{z0} \ll \tilde{q}_{x0,y0}$, so that

$$\tilde{q}_{x0}'' = \tilde{q}_{x0}, \tag{5}$$

$$\tilde{q}_{y0}'' = \tilde{q}_{y0}, \tag{6}$$

$$\tilde{q}_{z0}'' = \tilde{q}_{x0} \theta_1 - \tilde{q}_{y0} \theta_2 + \tilde{q}_{z0}. \tag{7}$$

We consider the reciprocal-lattice peak $\delta(\tilde{\mathbf{q}} - \tilde{\mathbf{q}}_0)$. This is located on the Ewald sphere for some $\omega = \omega_0$. By use of equations (4) and (7), we see that for the incident-beam component which deviates from the average collimation by θ_1, θ_2, this peak will be located on the Ewald sphere at $\omega = \omega_0 - \theta_1 + \tan(\tilde{\varphi})\theta_2$, with $\tilde{\varphi}$ the azimuthal position of the Bragg peak on the $\tilde{q}_x \tilde{q}_y$ plane; cf. equation (1). The intensity at the new rotation angle is proportional to $I_0(\theta)$, where $\theta = \cos^{-1}(\cos \theta_1 \cos \theta_2)$.[2]

The collimation-related part of the resolution function magnitude at some ω can be computed by numerical integration of the measured radial intensity profile $I_0(\theta)$ for all combinations of θ_1, θ_2 consistent with the constraint $\theta_1 - \tan(\tilde{\varphi})\theta_2 = \omega$:

---

[2] This is simply the angle between vector $\hat{\mathbf{z}}$ and vector $\hat{\mathbf{z}}''$, rotated by small angles θ_1 around $\hat{\mathbf{y}}$ and θ_2 around $\hat{\mathbf{x}}$.

$$R_c(\omega) = \int_{-\pi}^{\pi} \int_{-\pi}^{\pi} I_0[\cos^{-1}(\cos \theta_1 \cos\theta_2)]$$
$$\times \delta[\omega - \theta_1 + \tan(\tilde{\varphi})\theta_2] \, \mathrm{d}\theta_1 \, \mathrm{d}\theta_2. \tag{8}$$

4.2. Wavelength spread

The wavelength spread of the incident beam enters our analysis via the size of the Ewald sphere. We will incorporate this effect in the calculation of the resolution function, taking the case of a perfectly monochromatic beam at incident wavevector k_{in} as our starting point. We consider a δ peak in reciprocal space, the location of which is given by equation (1). This point is located on the Ewald sphere for rotation by the Bragg angle ω_0. In the beam-fixed (non-tilted) axes, the location of the δ peak satisfies

$$q_{x0}^2 + q_{y0}^2 + q_{z0}^2 = Q_0^2.$$

But it also belongs to the Ewald sphere, hence:

$$q_{x0}^2 + q_{y0}^2 + (q_{z0} + k_{in})^2 = k_{in}^2.$$

Combination of the above two relations leads to

$$q_{z0} = -Q_0^2/2k_{\mathrm{in}}.$$

Use of this expression and equation (4) leads to the relation determining the angle of rotation, ω_0:

$$\sin \omega_0 \cos \tilde{\varphi} \sin \tilde{\theta} - \cos \omega_0 \cos \tilde{\theta} = Q_0/2k_{\mathrm{in}}.$$

A slight variation of the incident wavevector (wavelength) by δk results in a variation of the necessary angle of rotation by $\delta\omega$:

$$(\cos \omega_0 \cos \tilde{\varphi} \sin \tilde{\theta} + \sin \omega_0 \cos \tilde{\theta}) \delta\omega = -\frac{Q_0}{2k_{\mathrm{in}}^2} \delta k.$$

This can be simplified, taking into account that in practice ω_0 is small and $\tilde{\theta}$ is almost $\pi/2$ [cf. discussion after equation (4)]:

$$\cos \tilde{\varphi} \, \delta\omega = -Q_0/2k_{\mathrm{in}}^2 \, \delta k.$$

The significance of the above is that for a non-monochromatic beam, the δ peak will give rise to diffracted intensity from neutrons of wavevector $k_{\mathrm{in}} + \delta k$ at rotation angle $\omega = \omega_0 + \delta\omega$. The intensity at angle ω is proportional to the incident beam intensity at wavelength $k_{\mathrm{in}} + \delta k$:

$$R_\lambda(\omega) \propto I_\lambda\left(k_{\mathrm{in}} - \frac{2k_{\mathrm{in}}^2 \cos \tilde{\varphi}}{Q_0} \omega\right), \tag{9}$$

where $I_\lambda(k)$ describes the distribution of wavelengths. In most cases, this is adequately approximated by a Gaussian peaked at k_{in}.

4.3. The combined effect

Finally, we compute the complete resolution function. We assume that the wavelength distribution is independent of the angular orientation of a certain segment of the neutron beam. This allows us to determine the resolution function as a convolution between the collimation and wavelength-spread parts:

$$R(\omega) = \int_{-\pi}^{\pi} R_c(\omega' - \omega) R_\lambda(\omega') \, \mathrm{d}\omega'. \tag{10}$$

In what follows we use measured forms that describe the beam intensity profile and wavelength spread to perform the integrations that yield $R_c(\omega)$ and $R(\omega)$ numerically.

5. Numerical evaluation of the resolution function

We performed SANS rocking-curve measurements on an FLL in a niobium single crystal on the NG-3 instrument at NCNR-NIST. The experimental findings are reported in detail elsewhere (Daniilidis *et al.*, 2007). Here we compute the resolution function starting from the instrumental configuration and compare the result with experimentally obtained curves which are at the resolution limit.

The neutron wavelength was set to 6.0 Å, with 14% FWHM (full width at half-maximum) wavelength spread. The wavelength distribution for these settings is well approximated by a Gaussian (Glinka *et al.*, 1998). Double pinhole collimation was used, with a source aperture of 50 mm, sample aperture 6.35 mm, and source-to-sample aperture distance 15.78 m. We obtained a direct measurement of the incident-beam profile on the SANS detector. The radial average *versus* angle $\alpha \equiv Q/k_{in}$ is shown in Fig. 3(*a*). This is well approximated by[3]

$$I(\alpha) = \frac{A}{1 + \exp[(|\alpha| - 1.62)/0.26]},$$

where here and in what follows the angles are expressed in mrad. After correcting for the finite sizes of the sample aperture and the detector elements (pixels), we obtain a corrected angular profile. This is estimated by

$$I_0(\theta) \propto \frac{1}{1 + \exp[(|\theta| - 1.17)/0.16]},$$

and it is shown by the red curve in Fig. 3(*b*). After performing the integration defined in equation (8), one obtains the results represented by the green points in Fig. 3(*b*). The result of the numerical integration is adequately described by the curve

$$R_c(\omega) \propto \frac{1}{1 + \exp[(|\omega| - 1.38)/0.29]}.$$

This is shown in black in Fig. 3(*b*). The functions I, I_0 and R_c are even in ω, and we only show them for positive values of the argument.

The wavevector distribution for the settings used will be Gaussian, centered around $k_0 = 1.047$ Å^{-1}, with FWHM of $0.14k_0$. This is described by

$$I_\lambda(k) \propto \exp\{-[(k - k_0)/0.084k_0]^2\},$$

with k expressed in Å^{-1}. Our measurements were performed at an applied magnetic field of 0.4 T, which corresponds to a scattering vector $Q_0 \simeq 8.9 \times 10^{-3}$ Å^{-1}. We will focus on a Bragg peak centered around $\tilde{\varphi} = \pi/4$. Then, following equation (9), the wavelength contribution to the resolution function is a Gaussian given by

$$R_\lambda(\omega) \propto \exp[-(\omega/0.51)^2].$$

Next, we can perform the integration of equation (10), to obtain the results shown in green in Fig. 3(*c*). This is the instrumental resolution function. The results are well fitted by the 'sharp cutoff' function

$$R(\omega) \propto \frac{1}{1 + \exp[(|\omega| - 1.38)/0.36]}.$$

The fit is shown by the black curve in Fig. 3(*c*). The sharp cutoff of $R(\omega)$ is a result of the box-shaped angular intensity profile $I(\alpha)$. We note that $R(\omega)$ is not adequately described by a Gaussian. A Gaussian fit deviates from the curve by as much as $0.06R(0)$.

The computed function slightly overestimates the width of the actual resolution function. For example, the rocking curves of an
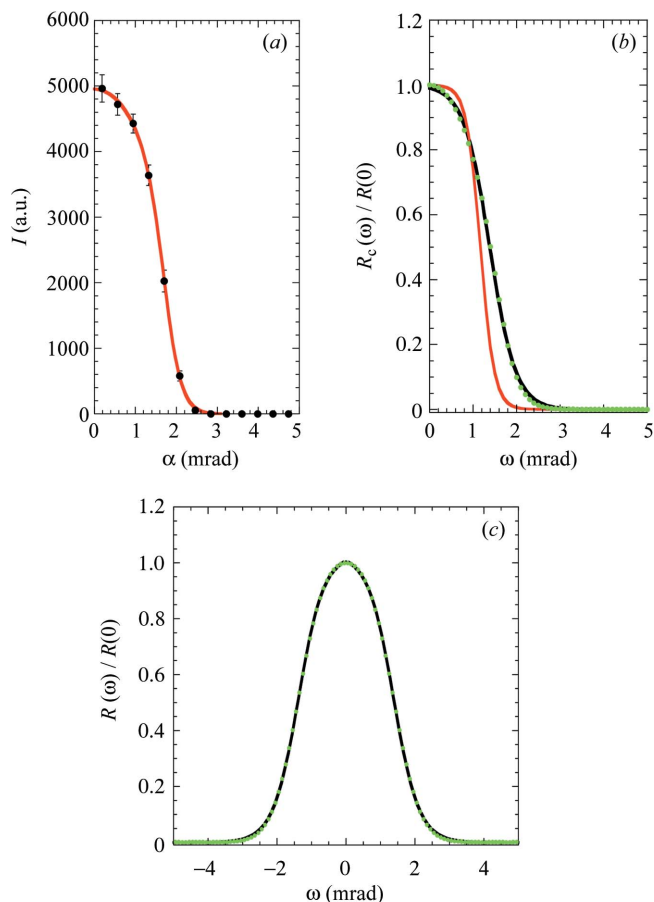
---

[3] The functional form $f(x) = A/\{1 + \exp[(x - x_0)/a]\}$ is used because it can adequately approximate box-shaped functions with a sharp cutoff around x_0.

Figure 3
(*a*) Direct-beam profile on the SANS detector *versus* $\alpha \equiv Q/k_{in}$, and fit through the data. (*b*) Red curve: direct-beam angular profile estimated from (*a*). Green–black curve: collimation contribution to the resolution function $R_c(\omega)$ (numerical integration, green points) and fit through the data (black curve), for a Bragg peak located at $\tilde{\varphi} = 45°$. (*c*) The end result for the resolution function $R(\omega)$ (green dots) and fit trough the data (black curve).

ordered FLL in niobium, obtained under the conditions introduced in our calculation, have half width of 1.2 mrad (Daniilidis *et al.*, 2007), which is approximately 87% of the width of the numerical integration result (1.38 mrad). This discrepancy is a result of the assumptions made in our calculation. We have assumed for simplicity that the neutron-beam intensity profile is azimuthally symmetric, while in reality it shows asymmetry of the order of 25% in different azimuthal directions. In addition, we assumed that the wavelength distribution in the beam is independent of the polar angle (θ) of the incident neutrons, whereas the two can be related.

6. Summary and conclusion

We have presented a method of calculating the resolution function for SANS rocking-curve measurements starting from the angular intensity profile and wavelength spread of the incident neutron beam. The result of this calculation is a slight overestimate of the actual resolution function. We also described the Ewald construction for SANS experiments from line-like objects, such as FLLs in type-II superconductors. The Ewald analysis provides a simple way to understand rocking-curve experiments from such systems.

References

Barker, J. G. & Pedersen, J. S. (1995). *J. Appl. Cryst.* **28**, 105–114.
Christen, D. K., Kerchner, H. R., Sekula, S. T. & Thorel, P. (1980). *Phys. Rev. B*, **21**, 102–117.
Cubitt, R., Forgan, E. M., Paul, D. McK., Lee, S. L., Abell, J. S., Mook, H. & Timmins, P. A. (1992). *Physica B*, **180–181**, 377–379.
Daniilidis, N. D., Park, S. R., Dimitrov, I. K., Lynn, J. W. & Ling, X. S. (2007). *Phys. Rev. Lett.* Submitted.
Forgan, E. M., Levett, S. J., Kealey, P. G., Cubitt, R., Dewhurst, C. D. & Fort, D. (2002). *Phys. Rev. Lett.* **88**, 167003.
Glinka, C. J., Barker, J. G., Hammouda, B., Krueger, S., Moyer, J. J. & Orts, W. J. (1998). *J. Appl. Cryst.* **31**, 430–445.
Harris, P., Lebech, B. & Pedersen, J. S. (1995). *J. Appl. Cryst.* **28**, 209–222.
Klein, T., Joumard, I., Blanchard, S., Marcus, J., Cubitt, R., Giamarchi, T. & LeDoussal, P. (2001). *Nature (London)*, **413**, 404–406.
Ling, X. S., Park, S. R., McClain, B. A., Choi, S. M., Dender, D. C. & Lynn, J. W. (2001). *Phys. Rev. Lett.* **86**, 712–715.
Lynn, J. W., Rosov, N., Grigereit, T. E., Zhang, H. & Clinton, T. W. (1994). *Phys. Rev. Lett.* **72**, 3413–3416.
Pedersen, J. S., Posselt, D. & Mortensen, K. (1990). *J. Appl. Cryst.* **23**, 321–333.
Ramakrishnan, V. (1985). *J. Appl. Cryst.* **18**, 42–46.
Roth, M. & Lewit-Bentley, A. (1982). *Acta Cryst.* A**38**, 670–679.
Schoenborn, B. P. (1983). *Acta Cryst.* A**39**, 315–321.
Yaron, U., Gammel, P. L., Huse, D. A., Kleiman, R. N., Oglesby, C. S., Bucher, E., Batlogg, B., Bishop, D. J., Mortensen, K., Clausen, K., Bolle, C. A. & De La Cruz, F. (1994). *Phys. Rev. Lett.* **73**, 2748–2751.